Medical Engineering and Physics 38 (2016) 1185–1194

Contents lists available at ScienceDirect

Medical Engineering and Physics

journal homepage: www.elsevier.com/locate/medengphy

Feedback control of electrical stimulation electrode arrays

C.T. Freeman*, K. Yang, J. Tudor, M. Kutlu

Electronics and Computer Science, Faculty of Physical Science and Engineering, University of Southampton, Southampton SO17 1BJ, UK

ARTICLE INFO

Article history:
Received 22 October 2015
Revised 3 June 2016
Accepted 4 July 2016

Keywords:
Electrode arrays
Electrical stimulation
Feedback control
Assistive technology

ABSTRACT

Electrical stimulation electrode arrays are an emerging technology that enables muscles to be artificially contracted through the activation of their associated motor neurons. A principal application of electrical stimulation is to assist human motion for orthotic or therapeutic purposes. This paper develops a framework for the design of model-based electrode array feedback controllers that balance joint angle tracking performance with the degree of disturbance and modeling mismatch that can exist in the true underlying biomechanical system. This framework is used to develop a simplified control design procedure that is suitable for application in a clinical setting. Experimental results evaluate the feasibility of the control design approach through tests on ten participants using both fabric and polycarbonate electrode arrays.

1. Introduction

There is a pressing need for novel technologies to support recovery of arm function following neurological conditions such as stroke and multiple sclerosis. Electrical stimulation (ES) uses electric impulses to artificially activate nerve cells causing muscle contraction, and has become an area of intense engineering and clinical research over the last few years [1–3]. By directly activating weak or paralyzed muscles, ES is able to drive neuroplastic cortical changes to enable recovery. ES is supported by a growing body of clinical evidence [4–6], and is increasingly combined with mechanical support, taking the form of either passive orthoses or active robots. These devices help support the affected limb using various training modalities, and therefore help reduce muscle fatigue or provide functionality that ES cannot (e.g. to assist with forearm supination or help stabilize the scapula).

The recent emergence of transcutaneous electrode arrays has potential to improve selectivity, automate placement, and reduce fatigue and discomfort compared with single pad ES electrodes [7,8]. The freedom they embed to adjust the size and shape of the electrode means they can isolate smaller muscle groups, and thereby enable the user to perform a variety of functional tasks including walking [9,10], and hand/wrist motion [8,11].

A major aim of current ES electrode array research is to produce a flexible, breathable, and light weight device that patients can use at home to support independent living. Manufacturing processes capable of realizing this form of wearable technology have recently been demonstrated: screen printing of bespoke polymer based pastes has been successfully used to produce a flexible and breathable fabric electrode array [12], with an example shown in Fig. 1. Screen printing is a straightforward and cost effective fabrication method which facilitates significant design freedom in terms of pattern geometries [13,14]. This technique has overcome limitations of alternative fabrication techniques: embroidery requires expensive high quality custom made silver sputtered yarns [15], and weaving and knitting constrains the array design layout to follow the physical location of the yarns [16–18] and has a lack of homogeneity in electrical properties.

However, lack of precise, clinically feasible methods with which to control the ES applied to the large number of electrode array elements remains a substantial challenge. Existing control strategies are open-loop and use time-consuming element selection procedures, which limits accuracy and usability. For example, in the report by Heller et al. [9], array elements are stimulated sequentially to locate the best single site for drop foot, obtaining similar performance to that produced manually by a clinician. Each array element is also tested in turn in Schill et al. [19], using simple criteria to assess the quality of wrist stabilization, with tests performed on tetraplegic spinal cord injury patients. Other implementations such as Keller et al. [20] also operate in a similar way to a clinician manually repositioning a single electrode. In the work by Popović and Popović [21] array electrodes are selected to minimize a cost function based on joint angle data produced during individual activation, and in the work by Malešević et al. [22] the same form of data is used to train an artificial neural network. There is therefore a clear need for model-based feedback control

* Corresponding author. Fax: +44 2380593709.
E-mail addresses: cf@ecs.soton.ac.uk (C.T. Freeman), ky2@ecs.soton.ac.uk (K. Yang), mjt@ecs.soton.ac.uk (J. Tudor), mck1e12@ecs.soton.ac.uk (M. Kutlu).

http://dx.doi.org/10.1016/j.medengphy.2016.07.002

Fig. 1. Screen printed fabric electrode array.

designs to improve accuracy, ideally embedding mechanisms to reduce the model identification time through selection of a reduced input search space. Control design in such a framework implicitly rests on a compromise between tracking accuracy of the nominal system and its robustness to model uncertainty. In order to reach this trade-off in a systematic manner, it is vital to employ a principled design procedure based on underlying theoretical performance and robustness results. To address this problem, the goal of this paper is two-fold:

1. We develop a comprehensive framework in which to design controllers to assist motion using ES electrode arrays. For the first time this establishes precise bounds on the level of modeling error that can be tolerated (e.g. due to muscle fatigue) and facilitates design of controllers that transparently balance tracking performance with robustness to such uncertainty and simplifications that enable clinically feasible identification methods to be employed.
2. We apply this framework to experimentally evaluate the performance of fabric electrode arrays with ten participants, and in particular compare achievable tracking accuracy with that of the leading alternative (arrays printed on polycarbonate with a hydrogel layer).

This paper exploits general robustness analysis developed by Freeman [23, Chapter 8] for ES control of the upper limb, but specifies them to array based linear feedback control. The significant simplification this unlocks enables more transparent results to be developed, which in turn lead to new control design procedures. This paper also contains far broader evaluation results, as well as a comparative study between two types of electrodes. The contents are organised as follows: Section 2 describes the model of the electrode array stimulated system, Section 3 develops a design framework for robust feedback controllers, and Section 4 presents a suitable model identification procedure. Experimental results are given in Section 5 and conclusions in Section 6.

2. Modeling of a single ES electrode array

Let signal $\boldsymbol{u} \in \mathcal{L}_2^n[0,T]$ contain the ES signals applied to each of the n elements of the array over time interval $t \in [0, T]$. The stimulation which then causes contraction of the ith muscle can be assumed to be a linear combination of those array elements within spatial range, and is therefore modeled by component

$$z_i(t) = \sum_{j=1}^{n} a_{i,j} u_j(t), \quad i = 1, \ldots, m, \quad t \in [0,T], \tag{1}$$

within signal $\boldsymbol{z} \in \mathcal{L}_2^m[0,T]$, where $a_{i,j} \in \mathbb{R}_+$ is the contribution of the jth array element. If the ith muscle acts about a single joint with angle $\phi_k(t)$, then the Hill type model states that the resulting moment is

$$\tau_{k,i}\big(z_i(t), \phi_k(t), \dot{\phi}_k(t)\big) = h_i(z_i(t), t) \times \tilde{F}_{M,k,i}\big(\phi_k(t), \dot{\phi}_k(t)\big) \tag{2}$$

where $h_i(z_i(t), t)$ is a Hammerstein structure comprising static non-linearity, $h_{IRC,\,i}(z_i(t))$, representing the isometric recruitment curve, cascaded with stable linear activation dynamics, $H_{LAD,\,i}$, represented by state-space triple $\{M_{A,\,i}, M_{B,\,i}, M_{C,\,i}\}$. Bounded term $\tilde{F}_{M,k,i}(\cdot)$ captures the effect of joint angle and angular velocity on the moment generated. As multiple muscles and/or tendons may each span any subset of joints, the general expression for the total moment generated about the kth joint can be represented by

$$\tau_k\big(z(t), \boldsymbol{\phi}(t), \dot{\boldsymbol{\phi}}(t)\big) = \sum_{i=1}^{m} \big\{ d_{k,i}(\phi_k) \times \tau_{k,i}\big(z_i(t), \phi_k(t), \dot{\phi}_k(t)\big) \big\}, \quad k = 1, \ldots p. \tag{3}$$

Here $d_{k,i}(\phi_k) = \frac{\partial E_i(\phi_k)}{\partial \phi_k}$ is the moment arm of the ith muscle with respect to the kth joint, where continuous function E is the associated excursion [24]. Resulting moment $\boldsymbol{\tau} \in \mathcal{L}_2^p[0,T]$ actuates the joints of the inter-connected anthropomorphic and mechanical/robotic support structure, with associated joint angle signal $\boldsymbol{\phi} \in \mathcal{L}_2^p[0,T]$. As demonstrated by Freeman [23, Chapter 2], this structure can be represented by the rigid body dynamic system

$$\boldsymbol{B}(\boldsymbol{\phi}(t))\ddot{\boldsymbol{\phi}}(t) + \boldsymbol{C}(\boldsymbol{\phi}(t), \dot{\boldsymbol{\phi}}(t))\dot{\boldsymbol{\phi}}(t) + \boldsymbol{F}(\boldsymbol{\phi}(t), \dot{\boldsymbol{\phi}}(t)) + \boldsymbol{G}(\boldsymbol{\phi}(t)) + \boldsymbol{K}(\boldsymbol{\phi}(t)) = \boldsymbol{\tau}(\boldsymbol{z}(t), \boldsymbol{\phi}(t), \dot{\boldsymbol{\phi}}(t)) \tag{4}$$

where $\boldsymbol{B}(\boldsymbol{\phi}(t))$ and $\boldsymbol{C}(\boldsymbol{\phi}(t), \dot{\boldsymbol{\phi}}(t))$ are respectively the $p \times p$ inertial and Coriolis matrices of the amalgamated anthropomorphic and mechanical/robotic support structure, and $\boldsymbol{G}(\boldsymbol{\phi}(t))$ is the $p \times 1$ combined gravity vector. The $p \times 1$ term $\boldsymbol{K}(\boldsymbol{\phi}(t))$ is the assistive moment produced by the mechanical passive/robotic support (see [23, Chapter 2] for explicit forms in both exoskeletal and end-effector cases). Finally, $\boldsymbol{F}(\boldsymbol{\phi}(t), \dot{\boldsymbol{\phi}}(t))$ is the $p \times 1$ vector representing joint stiffness, damping and friction effects, which for simplicity will be assumed to take the form

$$\boldsymbol{F}(\boldsymbol{\phi}(t), \dot{\boldsymbol{\phi}}(t)) = [F_{e,1}(\phi_1(t)) + F_{v,1}(\dot{\phi}_1(t)), \ldots, F_{e,p}(\phi_p(t)) + F_{v,p}(\dot{\phi}_p(t))]^\top. \tag{5}$$

Expansions in the form (5) can be made to incorporate more complex phenomena, e.g. those involving coupled position and velocity, or the addition of a varying set-point [25,26].

2.1. Operator description

The relationship between ES and joint angle defined by (1)–(5) can be expressed equivalently as

$$M : \mathcal{L}_2^n[0,T] \to \mathcal{L}_2^p[0,T] : \boldsymbol{u} \mapsto \boldsymbol{\phi} : \boldsymbol{\phi} = H_{RB} F_m(\boldsymbol{\phi}, \dot{\boldsymbol{\phi}}) H_{LAD} h_{IRC}(A\boldsymbol{u}), \tag{6}$$

with elements defined by the operators

$$A : \mathcal{L}_2^n[0,T] \to \mathcal{L}_2^m[0,T] : \boldsymbol{u} \mapsto \boldsymbol{z} : \boldsymbol{z}(t) = \begin{bmatrix} a_{1,1} & \cdots & a_{1,n} \\ \vdots & \ddots & \vdots \\ a_{m,1} & \cdots & a_{m,n} \end{bmatrix} \boldsymbol{u}(t),$$

$$\boldsymbol{h}_{IRC} : \mathcal{L}_2^m[0,T] \to \mathcal{L}_2^m[0,T] : \boldsymbol{z} \mapsto \boldsymbol{v} : \boldsymbol{v}(t) = [h_{IRC,1}(\boldsymbol{z}_1(t)), \ldots, h_{IRC,m}(\boldsymbol{z}_m(t))]^\top, \tag{7}$$

$$H_{LAD} : \mathcal{L}_2^m[0,T] \to \mathcal{L}_2^m[0,T] : \boldsymbol{v} \mapsto \boldsymbol{w} : \boldsymbol{w} = \begin{cases} \dot{\boldsymbol{x}}(t) = \begin{bmatrix} M_{A,1} & & \\ & \ddots & \\ & & M_{A,m} \end{bmatrix} \boldsymbol{x}(t) + \begin{bmatrix} M_{B,1} & & \\ & \ddots & \\ & & M_{B,m} \end{bmatrix} \boldsymbol{v}(t) \\ \boldsymbol{w}(t) = \begin{bmatrix} M_{C,1} & & \\ & \ddots & \\ & & M_{C,m} \end{bmatrix} \boldsymbol{x}(t) \end{cases}. \tag{8}$$

In addition, from (3) the muscle-joint moment operator is

$$F_m(\boldsymbol{\phi}, \dot{\boldsymbol{\phi}}) : \mathcal{L}_2^m[0,T] \to \mathcal{L}_2^p[0,T] : \boldsymbol{w} \mapsto \boldsymbol{\tau} : \boldsymbol{\tau}(t) = \begin{bmatrix} F_{M,1,1}(\boldsymbol{\phi}(t), \dot{\boldsymbol{\phi}}(t)) & \cdots & F_{M,1,m}(\boldsymbol{\phi}(t), \dot{\boldsymbol{\phi}}(t)) \\ \vdots & \ddots & \vdots \\ F_{M,p,1}(\boldsymbol{\phi}(t), \dot{\boldsymbol{\phi}}(t)) & \cdots & F_{M,p,m}(\boldsymbol{\phi}(t), \dot{\boldsymbol{\phi}}(t)) \end{bmatrix} \boldsymbol{w}(t) \tag{9}$$

where $F_{M,k,i}(\boldsymbol{\phi}(t), \dot{\boldsymbol{\phi}}(t)) = d_{k,i}(\phi_k) \times \tilde{F}_{M,k,i}(\phi_k(t), \dot{\phi}_k(t))$, and from (4) the rigid body dynamics operator is

$$H_{RB} : \mathcal{L}_2^p[0,T] \to \mathcal{L}_2^p[0,T] : \boldsymbol{\tau} \mapsto \boldsymbol{\phi} : \begin{cases} \dot{\boldsymbol{x}}(t) = \begin{bmatrix} \dot{\boldsymbol{\phi}}(t) \\ \boldsymbol{B}(\boldsymbol{\phi}(t))^{-1}(\boldsymbol{\tau}(t) - \boldsymbol{C}(\boldsymbol{\phi}(t), \dot{\boldsymbol{\phi}}(t))\dot{\boldsymbol{\phi}}(t) \\ \quad -\boldsymbol{F}(\boldsymbol{\phi}(t), \dot{\boldsymbol{\phi}}(t)) - \boldsymbol{G}(\boldsymbol{\phi}(t)) - \boldsymbol{K}(\boldsymbol{\phi}(t))) \end{bmatrix} \\ \boldsymbol{\phi}(t) = [\boldsymbol{I}, \boldsymbol{0}]\, \boldsymbol{x}(t), \end{cases} \tag{10}$$

Stimulated arm system (6) is sensitive to changes in array position, physiological variation (e.g. fatigue), and environmental conditions (e.g. temperature, humidity). This makes accurate identification of its parameters highly challenging, especially as methods involving sensing of force/moments around individual joints are impractical in a clinical setting if the system is used to model complex structures such as the hand. The next section quantifies the robustness of controllers designed using a nominal model which inevitably does not match the true plant.

3. Problem description

The stimulated arm control task is for joint angle output signal $\boldsymbol{\phi}$ to track a reference trajectory $\hat{\boldsymbol{\phi}} \in \mathcal{L}_2^p[0,T]$ by application of a suitable ES signal $\boldsymbol{u}$. To do this introduce the general feedback control operator

$$K : \tilde{\boldsymbol{e}} \mapsto \tilde{\boldsymbol{u}} : \mathcal{L}_2^p[0,T] \to \mathcal{L}_2^n[0,T], \tag{11}$$

implemented in the arrangement shown in Fig. 2, where $\boldsymbol{u}_0 \in \mathcal{L}_2^n[0,T]$ and $\boldsymbol{\phi}_0 \in \mathcal{L}_2^p[0,T]$ are external actuator and measurement disturbances respectively.

To reduce the number of degrees of freedom in the control problem we mimic the natural human motor control strategy which involves a single neural command signal controlling multiple muscles. Each group of muscles working together is called a synergy, and the same muscle can potentially be employed within multiple synergies. Denote the underlying neural signal by $\boldsymbol{r} \in \mathcal{L}_2^q[0,T]$ where $q \le m$, and let $\bar{X}_j \in \mathbb{R}^n$ be the array elements which make up the jth synergy. It follows that the map between neural and array stimulation signals is then $\boldsymbol{u} = X\boldsymbol{r}$, with

$$X : \mathcal{L}_2^q[0,T] \to \mathcal{X}[0,T] : \boldsymbol{r} \mapsto \boldsymbol{u},\ \boldsymbol{u}(t) = \underbrace{\left[\bar{X}_1 \ldots \bar{X}_q\right]}_{\bar{X} \in \mathbb{R}^{n \times q}} \boldsymbol{r}(t). \tag{12}$$

Setting $K = XK_X$ where $K_X : \boldsymbol{e} \mapsto \boldsymbol{r} : \mathcal{L}^p[0,T] \to \mathcal{L}^q[0,T]$ is a suitable feedback controller hence embeds synergies into the control action. In so doing, this structure restricts $\boldsymbol{u}$ to the convex subset $\mathcal{X}[0,T] := \left\{\boldsymbol{u} = X\boldsymbol{r},\ \boldsymbol{r} \in \mathcal{L}_2^q[0,T]\right\} \subset \mathcal{L}_2^n[0,T]$. Explicit forms of X and K_X will subsequently be derived.

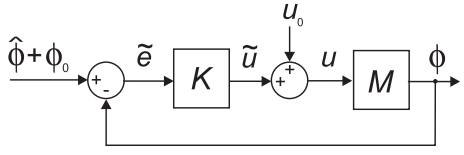

Fig. 2. Feedback system $[M, K]$ with controller K, external disturbances $\boldsymbol{u}_0$, $\boldsymbol{\phi}_0$ and nominal plant M: $\boldsymbol{u} \mapsto \boldsymbol{\phi}$.

3.1. Robust stability

The design objective for controller K is to stabilize plant model M and provide satisfactory tracking performance. However, all such models possess uncertainty and it is hence critical to examine the robust performance when K is applied to the true plant, denoted N, which may differ from M. To do this it is necessary to make the following assumption:

- The true rigid body dynamics are passive about their disturbance-free operating point, $(\bar{\boldsymbol{u}}_1, \bar{\boldsymbol{\phi}}_1)$. Here $\bar{\boldsymbol{u}}_1$, $\bar{\boldsymbol{\phi}}_1$ are respectively the plant input and output signals corresponding to the true system $[N, K]$ operating in the absence of external disturbance signals (i.e. $\boldsymbol{u}_0 = 0$, $\boldsymbol{\phi}_0 = 0$). In practice this assumption is either inherently satisfied by the form of anthropomorphic joint stiffness (5), or is ensured by appropriate selection and adjustment of the mechanical support (corresponding to the term $\boldsymbol{K}(\boldsymbol{\phi})$ in (4)).
- For simplicity we also assume that plant model M is linear, however the approaches described in this paper extend naturally to non-linear models and controller forms. For examples of the latter, the reader is referred to Chapter 3 of the textbook by Freeman [23].

We can now quantify the effect of modeling error on stability and performance of the true system $[N, K]$:

Theorem 3.1. *Let the linear control operator K be designed to stabilise plant model M. Then the true closed-loop system $[N, K]$ is bounded-input, bounded-output (BIBO) stable if*

$$\|N|_{\bar{\boldsymbol{u}}_1} - M\| < b_{M//K}^{-1} \tag{13}$$

where the 'gain margin' of the nominal system is given by

$$b_{M//K} = \left\| \begin{pmatrix} I \\ M \end{pmatrix} (I + KM)^{-1} (I, K) \right\| \tag{14}$$

and the modeling error is defined by

$$\|N|_{\bar{\boldsymbol{u}}_1} - M\| = \sup_{\|\boldsymbol{u}\| \neq 0} \frac{\|(N|_{\bar{\boldsymbol{u}}_1} - M)\boldsymbol{u}\|}{\|\boldsymbol{u}\|} \tag{15}$$

in which $N|_{\bar{\boldsymbol{u}}_1}\boldsymbol{u} = N(\boldsymbol{u} + \bar{\boldsymbol{u}}_1) - N\bar{\boldsymbol{u}}_1$. Furthermore the true tracking performance satisfies the bound

$$\left\| \begin{pmatrix} \boldsymbol{u} - \bar{\boldsymbol{u}}_1 \\ \boldsymbol{\phi} - \bar{\boldsymbol{\phi}}_1 \end{pmatrix} \right\| \le b_{M//K} \frac{1 + \|N|_{\bar{\boldsymbol{u}}_1} - M\|}{1 - b_{M//K}\|N|_{\bar{\boldsymbol{u}}_1} - M\|}. \tag{16}$$

Proof. See Appendix A. □

Theorem 3.1 shows that designing the controller K to reduce $b_{M//K}$ increases the set of true plants that can be stabilised. However, from components of (14) it is clear that a small $b_{M//K}$ strongly correlates with poorer tracking performance. This hence quantifies the usual trade-off existing between robustness and performance. Since N is never available to the designer, the practical utility of this theorem is to enable the designer to select K with a transparent understanding of how it affects the robustness of the closed-loop system. Numerous control methods can be employed to select

Table 1
Electrode array control design procedure for guaranteed robust stability.

Step (a) Stimulation subspace identification: use previous stimulation patterns, anatomical knowledge, or known geometric variation to define the set of synergies used by the controller. Use (12) to embed within the control operator X. This is addressed in Section 4.1.
Step (b) Biomechanical dynamics identification: identify a model M which captures the dynamics between ES input signal $\boldsymbol{u} \in \mathcal{X}[0,T]$ and resulting joint angular motion $\boldsymbol{\phi}$. More identification tests reduces mismatch, as defined by (A.3), but can never in practice fully characterize unpredictable time-varying dynamic effects. A suitable approach is given in Section 4.2.
Step (c) Feedback controller design: design K to stabilize M given the reduced stimulation subspace $\boldsymbol{u} \in \mathcal{X}[0,T]$, while providing satisfactory tracking accuracy. Taking the form $K = XK_X$, this is equivalent to designing K_X to stabilize MX. Section 3.2 develops a suitable controller.
Step (d) Examine robustness: calculate $b_{M//K}$ for above K form using (14). Substitute in Theorems 3.1 and 3.2 to inspect allowable model mismatch and its effect on robust performance. If not sufficiently robust, redesign K to reduce $b_{M//K}$. Note that multiple feedback controllers can be designed and one with a smaller $b_{M//K}$ can be switched in between task attempts if the system shows signs of instability.
Step (e) Reduce norm of H_{RB}, $F_m(\boldsymbol{\phi}, \dot{\boldsymbol{\phi}})$, H_{LAD}, $\boldsymbol{h}_{IRC}$: if controller performance is still poor, modify the system to reduce norm of terms in (17) which affect robustness margins (e.g. reduce ES levels, apply ES to actuate required joint angles, change mechanical structure and apply passive/active support). Then go to Step (b).

a form of K which stabilizes the system (i.e. produces a finite $b_{M//K}$) such as optimal control, H_∞ control, and pole-placement, while attaining a favorable balance between robustness and performance.

By substituting the underlying forms (7)–(10) into the left hand side of (13), Theorem 3.1 can also be used to bound the allowable modeling error in specific components of the plant model. The next example illustrates this approach.

Theorem 3.2. *Suppose the nominal model is constructed as* $M = \overline{H_{RB}F_m}H_{LAD}\bar{\boldsymbol{h}}_{IRC}$ *whose components are linear approximations to the true system* $N = H_{RB}F_mH_{LAD}\boldsymbol{h}_{IRC}$ *respectively. Then the true system* $[N, K]$ *has a robust stability margin, and in particular is stable if the modeling uncertainty satisfies*

$$\Delta_{IRC} < \frac{b_{M//K}^{-1} - \Delta_{RB}\|\bar{\boldsymbol{h}}_{IRC}\|}{\|H_{RB}F_m|_{\bar{\boldsymbol{w}}_1}\|} \quad \text{or} \quad \Delta_{IRC} < \frac{b_{M//K}^{-1} - \Delta_{RB}\|\boldsymbol{h}_{IRC}|_{\bar{\boldsymbol{z}}_1}\|}{\|\overline{H_{RB}F_m}\|}. \tag{17}$$

Here, the model uncertainty in the muscle recruitment curve and rigid body dynamics are respectively characterized by

$$\Delta_{IRC} = \max_i \|\boldsymbol{h}_{IRC,i}|_{\bar{\boldsymbol{z}}_{1,i}} - \bar{\boldsymbol{h}}_{IRC,i}\|, \quad \Delta_{RB} = \|H_{RB}F_m|_{\bar{\boldsymbol{w}}_1} - \overline{H_{RB}F_m}\|. \tag{18}$$

Proof. See Appendix B. □

Theorem 3.2 provides bounds on the modeling inaccuracy that can be tolerated in the various components of the assumed model M used for control design. Although components of the true plant are unknown to the designer, bounds on the uncertainty Δ_{RB}, Δ_{IRC} may be estimated by inspecting the fitting accuracy of the identified model, or by knowledge of how much these components vary over the course of a treatment session (e.g. using established variation in isometric recruitment curves due to fatigue [27]). Even if these bounds are not available to the designer, Theorem 3.2 provides valuable practical guidelines to aid controller design. For example, it shows how uncertainty bounds are affected by the size of other system components: to maximize the amount of uncertainty that can be tolerated requires designing K to reduce $b_{M//K}$ and, if possible, modifying the system to reduce $\|\bar{\boldsymbol{h}}_{IRC}\|$ and $\|\overline{H_{RB}F_m}\|$. Clearly undertaking control design based on linearised dynamics provides simplicity at the cost of reduced robustness margins. This cost increases with the degree of nonlinearity, as seen from the terms (18) which increase as $\boldsymbol{h}_{IRC,i}|_{\bar{\boldsymbol{z}}_{1,i}}$ and $H_{RB}F_m|_{\bar{\boldsymbol{w}}_1}$ differ from their respective linearised values. As well as yielding explicit robust performance bounds, the framework presented in this section directly leads to the guidelines for feedback control design given in Table 1.

3.2. Simplified system structure

Previously the controller form $K = XK_X$ was introduced to embed synergies and simplify model identification. This section illustrates the design of a suitable controller K_X, which appears in Step (c) of Table 1. It is first assumed that the plant model M identified in the preceding step is chosen to take the form $M = HF$, where F is the static $p \times n$ mapping operator

$$F : \mathcal{L}_2^n[0,T] \to \mathcal{L}_2^p[0,T] : \boldsymbol{u} \mapsto \boldsymbol{\psi} : \boldsymbol{\psi}(t) = \bar{F}\boldsymbol{u}(t), \ \bar{F} \in \mathbb{R}^{p\times n}, \tag{19}$$

and H embeds identical single input, single output (SISO) linear dynamics in each channel (i.e. $H : \boldsymbol{\phi}_i(s) = \bar{H}(s)\boldsymbol{\psi}_i(s)$ for SISO transfer-function $\bar{H}(s)$). This assumption is motivated by similar muscle activation and rigid body properties in the wrist and hand, together with stiffness, and the limited bandwidth required to complete the tracking task [23, Chapter 2]. Then a suitable design of K_X is given as follows:

Theorem 3.3. *Let the feedback control action* $K_X : \boldsymbol{e} \mapsto \boldsymbol{r} : \boldsymbol{r} = C(FX)^\dagger\boldsymbol{e}$, *where* C *embeds identical linear SISO dynamics in each channel, be applied to the system* $\boldsymbol{\phi} = MX\boldsymbol{r}$. *Then in the absence of disturbance* ($\boldsymbol{u}_0 = \boldsymbol{\phi}_0 = \boldsymbol{0}$) *this realizes the neural command signal*

$$\boldsymbol{r} = N_w\boldsymbol{r}^\star \tag{20}$$

where the signal $\boldsymbol{r}^\star \in \mathcal{L}_2^p[0,T]$ *minimizes the tracking error norm* $\|\boldsymbol{e}\|^2 = \|\hat{\boldsymbol{\phi}} - \boldsymbol{\phi}\|^2$ *with respect to* $\boldsymbol{r}$, *and the operator*

$$N_w := (I + CH)^{-1}CH. \tag{21}$$

The resulting closed-loop system dynamics are

$$\boldsymbol{\phi} = N_w(FX)^\perp\hat{\boldsymbol{\phi}} \tag{22}$$

where the orthogonal projection onto the range of FX *is* $(FX)^\perp = FX(FX)^\dagger : \mathcal{L}_2^p[0,T] \to \mathcal{L}_2^p[0,T] : \hat{\boldsymbol{\phi}} \mapsto \boldsymbol{x} : \boldsymbol{x}(t) = \bar{F}\bar{X}(\bar{F}\bar{X})^\dagger\hat{\boldsymbol{\phi}}(t)$.

Proof. See Appendix C. □

Selecting the feedback controller as $K = XK_X$ where $K_X = C(FX)^\dagger$ therefore forces $\boldsymbol{\phi}$ to track the demand input $\hat{\boldsymbol{\phi}}$ as closely as possible, subject to dynamics N_w specified by the designer. In particular, as N_w approaches unity, the control action generates neural signal $\boldsymbol{r}$ which equates to the minimum possible tracking error, i.e. solving $\min_{\boldsymbol{r}} \|\hat{\boldsymbol{\phi}} - \boldsymbol{\phi}\|^2$. Since M is linear, gain bound $b_{M//K}$ can be readily calculated using (14), to provide robust stability bounds for insertion in Theorems 3.1 and 3.2. Note that the assumed model and controller forms mean the bound can also be expressed as

$$b_{M//K} = \left\| \begin{pmatrix} I \\ FXH \end{pmatrix} (I + CH)^{-1} (I, C(FX)^\dagger) \right\|. \tag{23}$$

These bounds provide useful information to aid the designer in the selection of C within Theorem 3.3: as C increases N_w approaches unity and hence tracking accuracy is optimised, however $b_{M//K}$ also has the effect of increasing which reduces robustness. The designer must therefore employ standard control design methods to tune the characteristics of N_w, while ensuring (23) is not unduly large.

4. Model identification

The design procedure of Table 1 requires both the stimulation subspace map X and the biomechanical dynamics MX to be identified. The former is chosen directly by the designer and, depending on its size and specification, does not have to be changed.

In contrast, the latter is inevitably highly challenging to identify due to complex dynamics that include time-varying effects such as fatigue. The results in Section 3 allow the designer to trade-off robustness and tracking performance in their selection of K, and therefore reduce the need for accurate identification of MX (which may be infeasible in the case of the wrist and hand). To make identification of any form of model dynamics feasible in a clinical setting, appropriate selection of the stimulation subspace map X is needed to reduce the time needed to identify MX so that it can be performed within the limited time available in practice.

4.1. Stimulation subspace

In Step (a) of Table 1, stimulation subspace X can be constructed firstly by assembling a set of input data $\{\boldsymbol{x}^i\}$, $i = 1, \ldots, c$, with $\boldsymbol{x}^i \in \mathbb{R}^n$, comprising:

- *anatomical knowledge* (perhaps augmented by tests performed with a single electrode moved over the patient's arm). Here vector $\boldsymbol{x}^i$ specifies the electrode array elements that correspond to the ith muscle position (or alternatively can comprise a linear combination of muscle positions known to act together as a synergy), and/or
- *stimulation signals from previous experiments* (with any choice of input subspace) that resemble the required movements. Here vectors $\boldsymbol{x}^i$ are produced by taking a suitable sampling of each previous stimulation signal.

We then set

$$\bar{X} = [\boldsymbol{x}^1, \boldsymbol{x}^2, \ldots, \boldsymbol{x}^c] \in \mathbb{R}^{n \times c} \tag{24}$$

in (12) to produce X. This form guarantees the stimulation subspace contains the muscle patterns, synergies, and set of previously successful inputs. The number of components c defines the subspace dimension since $c = q$, however the designer may wish to independently prescribe q in order to reduce this dimension and thereby shorten the subsequent tests needed to identify MX. This can be achieved by employing factorization procedures that are described elsewhere [28], with this reference also containing all necessary computations.

4.2. Electrically stimulated biomechanical dynamics

Having determined X, Step (b) of Table 1 then requires that the biomechanical dynamics MX be identified. The problem of identifying this system model can be stated as follows:

$$MX = \arg \min_{\Lambda : \mathcal{L}_2^q[0,T] \to \mathcal{L}_2^p[0,T]} J(\Lambda), \quad J(\Lambda) = \| \Delta\boldsymbol{\phi} - \Lambda \Delta\boldsymbol{r} \|^2. \tag{25}$$

Here $\boldsymbol{r} = \bar{\boldsymbol{r}} - \Delta\boldsymbol{r}$, $\boldsymbol{\phi} = \bar{\boldsymbol{\phi}} - \Delta\boldsymbol{\phi}$ are the experimental input and output signals, with $\{\Delta\boldsymbol{r}, \Delta\boldsymbol{\phi}\} \in \mathcal{L}_2^q[0,T] \times \mathcal{L}_2^p[0,T]$, chosen to excite the system dynamics about an appropriate operating point $\bar{\boldsymbol{u}} = X\bar{\boldsymbol{r}}$. Many methods are available to solve (25), each of which benefit from the reduced input subspace $\mathcal{X}$ resulting from the presence of X. The selected method must be fast, sufficiently exciting, and comfortable for the patient.

Simplification is possible by using tests in which only one channel of $\boldsymbol{r}$ is varied at a time. This requires q tests, where in the ith test a signal $\boldsymbol{r}^i \in \mathcal{L}_2^q[0,T]$ is applied whose ith input channel is $\boldsymbol{r}_i^i = \bar{\boldsymbol{r}}_i - \Delta\boldsymbol{r}_i^i$, while the remaining input components are fixed at $\bar{\boldsymbol{r}}_j$, $j \neq i$. To guarantee sufficient excitation of dynamics, it is advisable to apply the maximum range of stimulation possible, $\boldsymbol{u}_{width}$, which can then be translated to the neural signal $\boldsymbol{r}$ using $\boldsymbol{r}_{i,width} = \|\bar{X}_i\|_\infty^{-1} \boldsymbol{u}_{width}$. The zero entries in $\Delta\boldsymbol{r}^i$ mean that (25) is replaced by the q lower order subproblems

$$(MX)_i = \arg \min_{\Lambda_i : \mathcal{L}_2[0,T] \to \mathcal{L}_2^p[0,T]} J(\Lambda_i), \quad J(\Lambda_i^i) = \left\| \Delta\boldsymbol{\phi}^i - \Lambda_i \Delta\boldsymbol{r}_i^i \right\|^2 \tag{26}$$

with $\Delta\boldsymbol{\phi}^i \in \mathcal{L}_2^p[0,T]$ the output of test i relative to the operating point $\bar{\boldsymbol{\phi}}$. Each of the q tests hence provides the component of MX corresponding to the channel being stimulated in that test.

Further simplification occurs if M is selected to have the particular form assumed in Theorem 3.3, in which case a suitable procedure is given in Table 2. Note that (28) corresponds to the 'line of best fit' when $\boldsymbol{\xi}_i^i$ is plotted against $\boldsymbol{\phi}_j^i$. Hence the approach corresponds to approximating the response of the j^{th} output to the single varying input, by a straight line, thus reducing the effect of noise in a transparent manner. This can be seen clearly when $\Delta\boldsymbol{r}_i^i$ is chosen to consist of straight line segments, as shown in Fig. 3, which also has the advantage of providing a smooth input for the patient, while covering the necessary $\boldsymbol{r}_{i,width}$ to ensure sufficient dynamic excitation.

5. Experimental results

The subspace selection, identification and control design procedures are now tested in a clinically relevant setting. The data acquisition system comprised real-time hardware (dSPACE ds1103) communicating with a graphical user interface (implemented using Matlab R14) running on the host PC. The hardware generated four 5 V 40 Hz square pulse trains whose pulsewidth was the controlled variable (0–300 μs). The voltage of each signal was then amplified by a modified commercial four channel voltage-controlled stimulator (Odstock Medical Ltd, UK). The resulting bi-polar signals could each be routed to any subset of electrodes within the $n = 24$ array via a RS232 controlled multiplexor (constructed using an Arduino board and shift register array). A separate 5 cm × 5 cm electrode was used as a common anode for all elements of the array, and was positioned over the styloid process of the ulna, at a distance of approximately 2 cm from the array. Two non-contact sensors (Kinect and PrimeSense) were used to measure wrist flexion/extensor, wrist abduction/adduction, and flexion of the metacarpophalangeal and proximal interphalangeal joints of each finger and the thumb, giving a total of $p = 12$ joint angles. These were computed as trigonometric functions of their associated Cartesian joint positions. To examine sensor efficacy, joint error was previously recorded while performing a range of hand gestures, and performance was quantified through comparison with a goniometer. A minimum mean joint error of less than 10° was established with the Kinect placed at 45° on the opposite side of the impaired arm at a −20° pitch angle in sitting mode, and the PrimeSense positioned 700 mm above the touch-table. Further details of the angle definitions and hardware appear in Chapter 9 of the text by Freeman [23].

Following University of Southampton ethical approval, ten unimpaired participants (6 men and 4 women) were recruited and gave written consent. Participants are denoted P1–P10 and their ages ranged from 32 to 67 years. Each participant was instructed to provide no voluntary effort, and this was confirmed prior to each test using surface electromyography (EMG) measurement. Tests were performed using the 4 × 6 element fabric electrode array shown in Fig. 1 and described in the report by Yang et al. [12]. To enable comparison, tests were also performed using the 4 × 6 element polycarbonate substrate array shown in Fig. 4 which has a hydrogel interface layer. This has identical dimensions to the fabric array, is manufactured by Tecnalia-Fatronik, San Sebastian, Spain, and is described elsewhere [10]. Each array was positioned as shown in Fig. 4(a), to cover wrist and finger extensor muscles. Identical placement of each array was achieved by marking the position of the initial array with microporous tape, and using this tape to align the subsequent array. At the beginning of each test session the stimulator amplitudes were set by routing one channel to two adjacent array elements, outputting a

Table 2
Simplified model identification procedure.

Step (i) Select an operating point $\{\bar{\boldsymbol{\phi}}, \bar{\boldsymbol{r}}\}$ which is as close to the desired movement or gesture as possible. Then perform q experimental tests, where in the ith test a varying signal $\Delta \boldsymbol{r}_i^i$ is superimposed onto the ith channel of neural signal $\bar{\boldsymbol{r}}$. Record the resulting joint angle perturbation this produces with respect to $\bar{\boldsymbol{\phi}}$, computed using $\Delta \boldsymbol{\phi}^i = \bar{\boldsymbol{\phi}} - \boldsymbol{\phi}^i$.

Step (ii) H: for any or all i, j, fit a SISO transfer-function $\bar{H}(s)$ to the pair of signals $\{\Delta \boldsymbol{\phi}_j^i, \Delta \boldsymbol{r}_i^i\}$. This is embedded in each channel of the operator H (i.e. $H : \boldsymbol{\phi}_i(s) = \bar{H}(s)\boldsymbol{\psi}_i(s)$). The most appropriate pair to use are those with largest magnitude.

Step (iii) FX: the required Λ has form $MX = HFX$ where H is now known. Since H has identical dynamics and FX is a static mapping, the position of H can be changed subject to the trivial modification of its number of identical channels. We hence write $MX = FXH$ and introduce the intermediate signal $\boldsymbol{\xi} = H\boldsymbol{r}$. It follows that the $MX = FX\boldsymbol{\xi}$ and identification problem (26) reduces to the static mapping problem

$$(FX)_i := \arg \min_{\Lambda_i : \mathcal{L}_2[0,T] \to \mathcal{L}_2^p[0,T]} J(\Lambda_i), \quad J(\Lambda_i) = \left\| \Delta \boldsymbol{\phi}^i - \Lambda_i \boldsymbol{\xi}_i^i \right\|^2. \tag{27}$$

where the signal $\boldsymbol{\xi}_i^i(s) = \bar{H}(s)\Delta \boldsymbol{r}_i^i(s)$. The solution to (27) is given by

$$(\bar{FX})_{i,j} = (\Xi^* \Xi)^{-1} \Xi^* \Delta \boldsymbol{\phi}_j^i \tag{28}$$

where $\Xi : \mathbb{R} \to \mathcal{L}_2[0,T] : \boldsymbol{a} \mapsto \boldsymbol{b} : \boldsymbol{b} = \boldsymbol{\xi}_i^i(t)\boldsymbol{a}$.

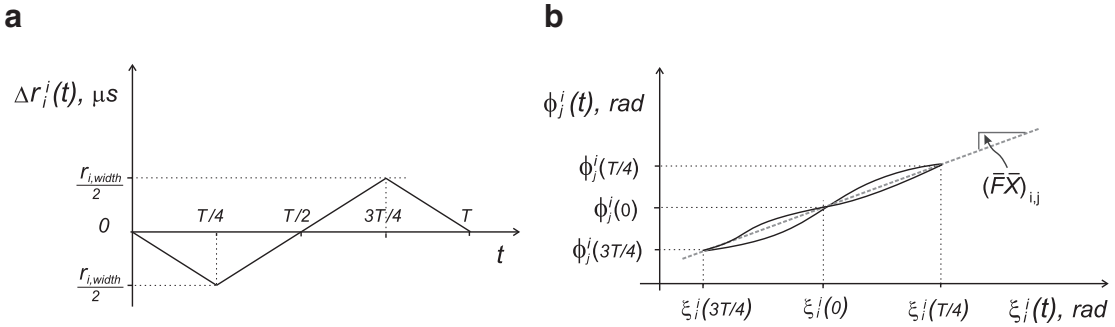

Fig. 3. Signals on ith test: (a) applied perturbation about the operating-point used to produce the applied stimulation: $\Delta \boldsymbol{r}_j^i = \bar{\boldsymbol{r}}_i - \boldsymbol{r}_i^i$, and (b) jth joint angle output plotted against the intermediate signal $\boldsymbol{\xi}_i^i(s) = \bar{H}(s)\Delta \boldsymbol{r}_i^i(s)$. Computing over all joints results in the identified model component $(\bar{FX})_i$.

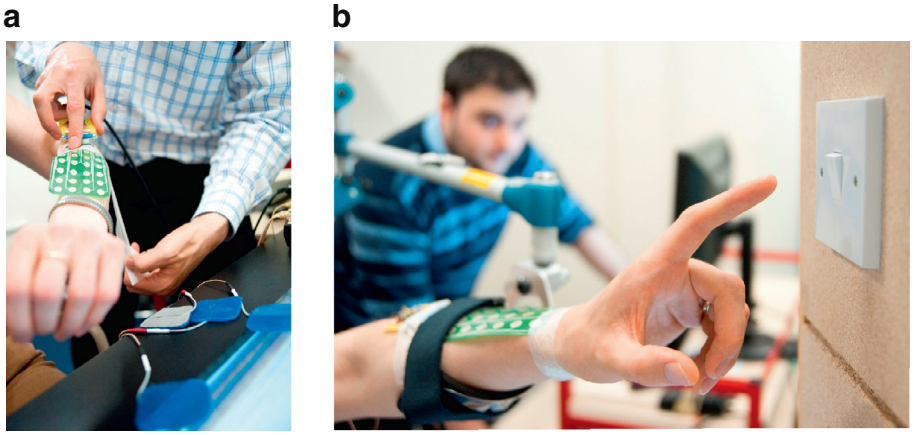

Fig. 4. (a) Electrode array (4 × 6 elements) being positioned on participant's forearm, subsequent to (b) the performing of a pointing task.

300 μs ($= \boldsymbol{u}_{width}$) signal and slowly increasing the amplitude until a maximum comfortable level was reached. The amplitudes of the remaining channels were set to identical levels. The stimulation signal pulsewidth of each channel is the controlled variable and combines with the routing hardware to realize electrode array ES signal $\boldsymbol{u}$. Each test started from a wrist angle of approximately 20° flexion, 0° abduction, and finger joint angles of 35° flexion, 0° abduction.

Three reference postures were employed; "pointing" with the index finger, a "pinch" hand posture and an "open" hand posture. These postures each involve wrist angle extension of approximately 60° relative to the initial starting position, and extension of the two joint angles of each finger by 25° for one or more fingers. In addition, the open posture involved abduction of each finger by approximately 15°. These led to three reference signals, $\hat{\boldsymbol{\phi}} \in \mathcal{L}_2^p[0,T]$, $T = 12$, with examples of the final gestures shown in Fig. 5. After tests were completed with one array type, the participant had a 30 min interval before tests were repeated with the other array type.

5.1. Unrestricted stimulation space

The control design procedure of Table 1 was applied using an unrestricted subspace in Step (a), formed by setting $q = n$, $\bar{X} = I$ in (12). In Step (b) the identification procedure of Table 2 was used to determine the components H and F within the assumed form $M = HF$. This procedure involved sequentially applying the ramp input shown in Fig. 3(b) to each of the $n = 24$ array elements in turn, while the $p = 12$ angular outputs were recorded. The duration of each identification test was 5 s with a sampling time of $T_s = 0.01$ s. For simplicity, a zero set-point ($\bar{\boldsymbol{r}} = \boldsymbol{0}$) was selected. In Step (c), the controller form of Theorem 3.3 was employed, with $C(s)$ taking the form of a PD controller (i.e. $C(s) = K_p + K_d s$, yielding overall control action $K(s) = XC(s)(FX)^{\dagger}$). Typical gains were selected so that

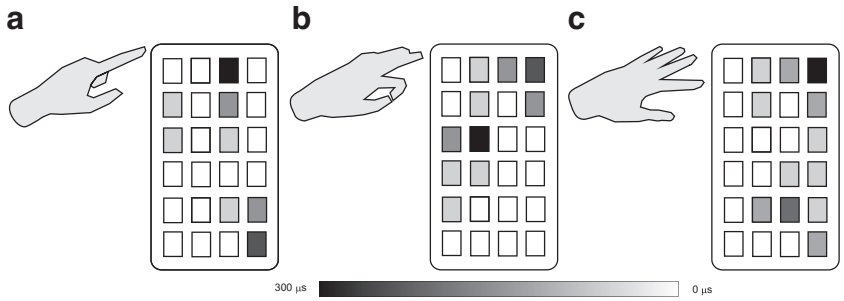

Fig. 5. Stimulation patterns for (a) pointing, (b) pinching and (c) open hand gestures.

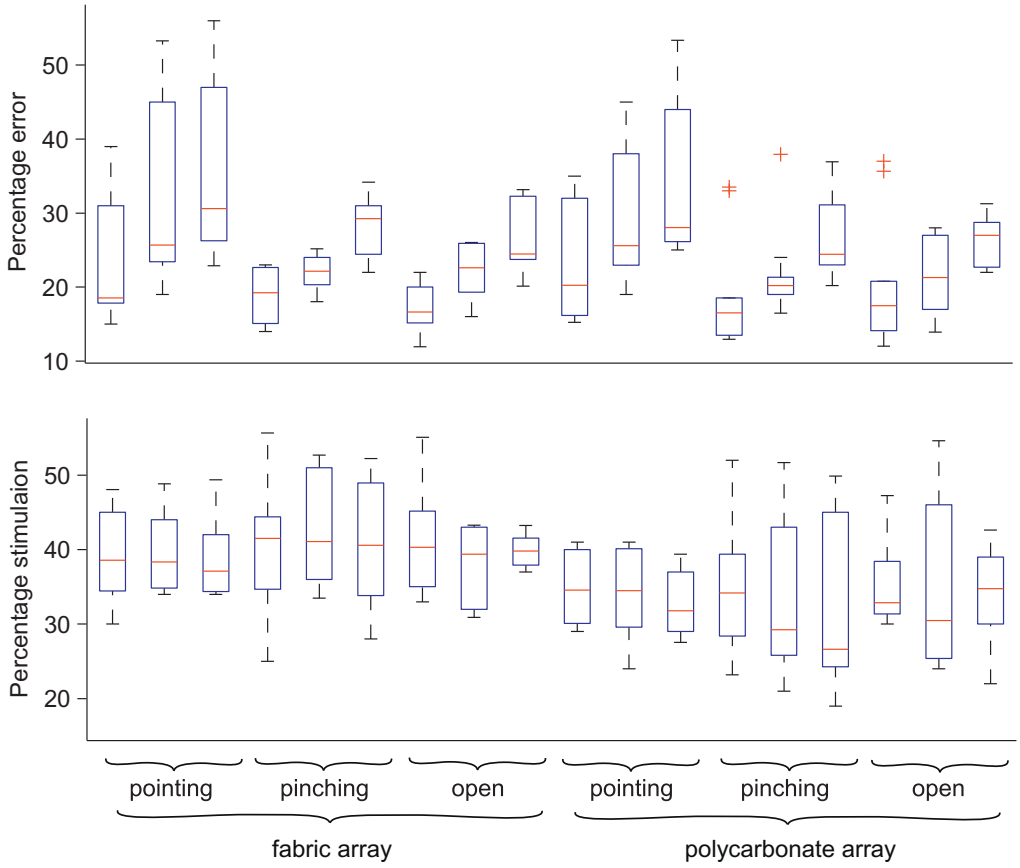

Fig. 6. Box plots showing percentage error and stimulation for three gestures and both array types. For each array type and gesture, the three box-plots shown correspond to: unrestricted subspace (left), task-specific restricted subspace (middle), task-independent restricted subspace (right).

$N_w(s)$ approximated a pure time delay, with example values for P1 being $K_p = 1.6$, $K_d = 0.4$. Substituting M and K into (14) produced a gain margin of $b_{M//K} = 1.6$ for P1. When K is applied to the true hand and wrist dynamics N, it follows from (A.3) that the resultant closed loop system $[N, K]$ is stable if $\|N|_{\tilde{\boldsymbol{u}}_1} - M\| < 0.625$. This constrains the true plant to a 'ball' in the uncertainty space with radius 0.625, centered on M. To quantify the tracking accuracy, percentage error was calculated across all joints for each posture using $100 \times \|\boldsymbol{e}\|/\|\boldsymbol{e}_0\|$, where $\boldsymbol{e} = \hat{\boldsymbol{\phi}} - \boldsymbol{\phi}$ and $\boldsymbol{e}_0 = \hat{\boldsymbol{\phi}} - \boldsymbol{\phi}_0$, with $\boldsymbol{\phi}_0$ the initial posture prior to stimulation. Similarly, percentage stimulation was computed using $100 \times \|\boldsymbol{u}\|/\|\boldsymbol{u}_{max}\|$ where $\boldsymbol{u}_{max}$ is the maximum possible stimulation (equating to a continuous input of 300 μ s applied to all channels). Results are shown in Fig. 6 averaged across two repetitions of each task. Fig. 5 shows the stimulation sites corresponding to $\boldsymbol{u}$ across each task for P1. Note that, due to the hardware only being able to generate 4 channels of stimulation, an additional (non-convex) projection operator was applied to the output of the controller to insure that each stimulation signal was either zero or one of only four non-zero levels at each time point. This projection is detailed in the work by Freeman [28].

5.2. Stimulation subspace

Each participant took a rest period of 30 min following the previous tests. For each participant a restricted stimulation subspace was then employed in Step (a) of Table 1 to speed up the test procedure. For simplicity the subspace was constructed by combining 4 experimental data sets, $\{\boldsymbol{u}^i\}$, $i = 1, \ldots, 4$, that were found to produce low tracking error norms in Section 5.1. Subspace X was hence constructed by setting $\boldsymbol{x}^i = \boldsymbol{u}^i$ and inserting in (24), leading to $q = 4$. Then, in Step (b), the identification proce-

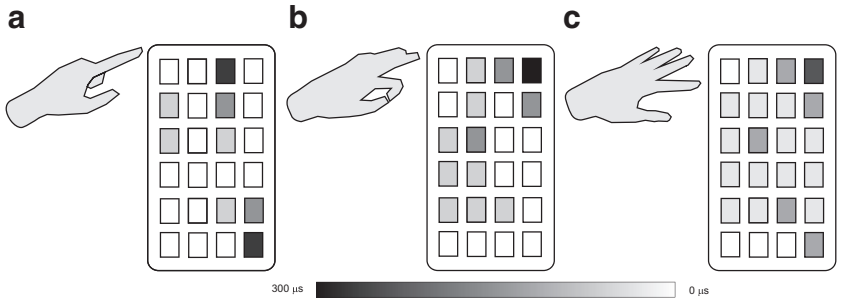

Fig. 7. Stimulation pattern approximations to those of Fig. 5, generated using a restricted subspace of dimension 2. As previously these correspond to (a) pointing, (b) pinching and (c) open hand gestures.

dure of Table 2 required only 4 tests instead of 24. In Step (c) the controller form of Theorem 3.3 was again employed with $C(s)$ taking the form of a PD controller. Percentage error norm values are given in Fig. 6 (denoted 'task-specific restricted subspace') and show only a small reduction in accuracy, while the identification test time is reduced to 20 s.

The previous results require a separate subspace X to be calculated for each task. A single subspace for all three tasks with dimension $q = 6$ was computed for each participant using the matrix factorization approach described in Section 4.1. Results for this task-independent restricted subspace are shown in Fig. 6. With only a small drop in accuracy this subspace covers a wide range of functional tasks, and corresponds to an identification test time of 30 s (equating to 6 tests in Step (i) of Table 2).

To illustrate the operation of the matrix factorization approach, consider the following, simpler, example: suppose a subspace with dimension two is required for the three stimulation patterns shown in Fig. 5. Computation in the same manner as above (using Matlab function `nnmf` as described in [28]) yields the necessary 24×2 matrix $\bar{X}$, restricting the possible stimulation patterns to the form $\boldsymbol{u}(t) = \bar{X}\boldsymbol{r}(t)$, where $\boldsymbol{r}(t)$ has only two elements. If these two elements are chosen to try and achieve each of the three original movements of Fig. 5, then the closest possible approximations are shown in Fig. 7. It is clear that reasonable accuracy has been possible in this case, due to the shared features present in these stimulation patterns.

5.3. Discussion

To examine the effect of experimental parameters, a three way analysis of variance (ANOVA) was conducted on the data (using SPSS Statistics V22.0). Here the independent variable was percentage error and the three factors were: gesture (pointing; pinching; open), array type (fabric; polycarbonate) and subspace (unrestricted; restricted; particpant-specific). Main effect analysis showed that the subspace significantly affected percentage error ($p = 0.000$). In addition the gesture had a significant affect on percentage error ($p = 0.045$). However the main affect of array type did not have a significant effect on percentage error, nor any of its interactions.

Next the independent variable was changed to percentage stimulation, and the ANOVA repeated using the same factors. In this case main effect analysis showed that the subspace significantly affected percentage stimulation ($p = 0.022$). In addition the array type had a significant affect on percentage stimulation ($p = 0.000$). However the main affect of task did not have a significant effect on percentage stimulation.

These results confirm that both electrode types yield similar levels of tracking accuracy, however, fabric arrays require greater levels of stimulation pulsewidth to achieve the same accuracy. This is due to the stimulator used, which has a voltage-driven output stage, together with the slightly increased impedance of the fabric array. It is clear that the effect of control parameters (i.e. underlying subspace) exerts a far more pronounced effect on performance.

6. Conclusions

This paper has developed a robust control design framework for electrode array based stimulation. A restricted stimulation subspace has first been proposed to enable identification to be performed quickly, making it feasible for use in clinical practice. Then robust performance bounds were derived which allowed performance and robustness to be balanced in a transparent, principled manner, giving rise to a pragmatic control design procedure. The utility of the framework was then illustrated through the development of a simplified model and associated control design procedure that was shown to provide satisfactory tracking accuracy with ten unimpaired participants in tests using both fabric and polycarbonate electrode arrays. The identification procedure was quick and easy to apply, and the feedback controller had a simple structure that could be transparently tuned by the designer to trade-off tracking accuracy and robustness to mode uncertainty.

A limitation in the results presented in this section is that testing was performed only with functional participants. Involuntary reflex responses to ES exist in unimpaired participants that may be absent in some stroke participants, and thereby produce inconsistencies in dynamic behavior between these two groups. Although an attempt to detect and minimize voluntary contribution to movement was employed in the experimental procedure, this cannot be completely discounted. Other differences in these groups include the presence of muscle weakness and increased stiffness in stroke participants. Although these will be captured in the identification procedure of Table 2, they may lead to more rapid degradation in performance.

Future work will center on evaluating the controllers with stroke participants. Here the same experimental procedure as described in this paper will be employed, including comparing the performance of fabric and polycarbonate electrode arrays. Future technical development will address the dual problems of: (1) reducing or eliminating the need for explicit model identification tests, and (2) maintaining performance despite time-variation in the dynamics of the stimulated limb. A possible avenue will be to use the model, controller and robustness bounds developed in this paper within the estimation based multiple model switched adaptive control (EMMSAC) framework of Freeman et al. [29]. This framework is based on prescribing a (possibly very large) number of plant models that may capture the dynamics of the stimulated limb, and designing a controller for each one. The controller that corresponds to the most accurate model at any time (as measured by an estimator) is automatically switched into closed-loop. By adapting to both slow and fast variations in dynamics, the

EMMSAC framework has potential to maintain high accuracy in the presence of fatigue and physiological variation.

Acknowledgment

This work was supported by the Engineering and Physical Sciences Research Council (EPSRC) Grant no. EP/M026388/1. Ethics Approval was given by University of Southampton Ethics and Research Governance Online (ERGO), ID 7710. All data supporting this study are openly available from the University of Southampton e-Prints repository at DOI: 10.5258/SOTON/396293.

Appendix A. Proof of Theorem 3.1

The assumption on passivity in Section 3.1 is equivalent to satisfying over $t \in [0, T]$

$$(\boldsymbol{\phi}(t) - \bar{\boldsymbol{\phi}}_1(t))^\top \left(\boldsymbol{F}_e(\boldsymbol{\phi}(t)) + \boldsymbol{G}(\boldsymbol{\phi}(t)) + \boldsymbol{K}(\boldsymbol{\phi}(t)) - \bar{\boldsymbol{\tau}}_1(t)\right) \geq 0 \tag{A.1}$$

where $\bar{\boldsymbol{\tau}}_1 = \boldsymbol{\tau}(A\bar{\boldsymbol{u}}_1, \bar{\boldsymbol{\phi}}_1, \dot{\bar{\boldsymbol{\phi}}}_1)$. Here the operating points can be formally defined as $\begin{pmatrix}\bar{\boldsymbol{u}}_1\\ \bar{\boldsymbol{\phi}}_1\end{pmatrix} = \Pi_{N//K}\begin{pmatrix}\boldsymbol{0}\\ \hat{\boldsymbol{\phi}}\end{pmatrix}$ where the projection operator $\Pi_{N//K} : \begin{pmatrix}\boldsymbol{u}_0\\ \hat{\boldsymbol{\phi}}+\boldsymbol{\phi}_0\end{pmatrix} \mapsto \begin{pmatrix}\boldsymbol{u}\\ \boldsymbol{\phi}\end{pmatrix}$. Likewise (A.1) is assumed to hold for the modeled plant about operating point $(\bar{\boldsymbol{u}}, \bar{\boldsymbol{\phi}})$ where $\begin{pmatrix}\bar{\boldsymbol{u}}\\ \bar{\boldsymbol{\phi}}\end{pmatrix} = \Pi_{M//K}\begin{pmatrix}\boldsymbol{0}\\ \hat{\boldsymbol{\phi}}\end{pmatrix}$ where the projection operator $\Pi_{M//K} : \begin{pmatrix}\boldsymbol{u}_0\\ \hat{\boldsymbol{\phi}}+\boldsymbol{\phi}_0\end{pmatrix} \mapsto \begin{pmatrix}\boldsymbol{u}\\ \boldsymbol{\phi}\end{pmatrix}$. It is then shown in [23, Chapter 3] that this condition guarantees the existence of a surjective map, $\Psi\begin{pmatrix}\boldsymbol{u}+\bar{\boldsymbol{u}}\\ M(\boldsymbol{u}+\bar{\boldsymbol{u}})\end{pmatrix} = \begin{pmatrix}\boldsymbol{u}+\bar{\boldsymbol{u}}_1\\ N(\boldsymbol{u}+\bar{\boldsymbol{u}}_1)\end{pmatrix}$, between graphs of the modeled and true systems, $\mathcal{G}_M$ and $\mathcal{G}_N$ respectively, defined by

$$\mathcal{G}_M := \left\{ \begin{pmatrix}\boldsymbol{u}\\ \boldsymbol{\phi}\end{pmatrix} : \left\| \begin{pmatrix}\boldsymbol{u}\\ \boldsymbol{\phi}\end{pmatrix} \right\|_{\begin{pmatrix}\bar{\boldsymbol{u}}\\ \bar{\boldsymbol{\phi}}\end{pmatrix}} < \infty,\ \boldsymbol{\phi} = M\boldsymbol{u} \right\},$$

$$\mathcal{G}_N := \left\{ \begin{pmatrix}\boldsymbol{u}\\ \boldsymbol{\phi}\end{pmatrix} : \left\| \begin{pmatrix}\boldsymbol{u}\\ \boldsymbol{\phi}\end{pmatrix} \right\|_{\begin{pmatrix}\bar{\boldsymbol{u}}_1\\ \bar{\boldsymbol{\phi}}_1\end{pmatrix}} < \infty,\ \boldsymbol{\phi} = N\boldsymbol{u} \right\}.$$

This enables the well-established gap metric to be applied to quantify the modeling uncertainty [30], defined as

$$\vec{\delta}(M, N) := \inf \left\{ \|(\Psi - I)_{\mathcal{G}_M}\|_{\begin{pmatrix}\bar{\boldsymbol{u}}\\ \bar{\boldsymbol{\phi}}\end{pmatrix}} : \Psi \text{ is a causal, surjective map from } \mathcal{G}_M \text{ to } \mathcal{G}_N \text{ with } \Psi\begin{pmatrix}\bar{\boldsymbol{u}}\\ \bar{\boldsymbol{\phi}}\end{pmatrix} = \begin{pmatrix}\bar{\boldsymbol{u}}_1\\ \bar{\boldsymbol{\phi}}_1\end{pmatrix} \right\}, \tag{A.2}$$

This gap metric is shown in [23, Chapter 3] to have an upper bound given by

$$\vec{\delta}(M, N) \leq \sup_{\|\boldsymbol{u}\| \neq 0} \frac{\|(N|_{\bar{\boldsymbol{u}}_1} - M|_{\bar{\boldsymbol{u}}})\boldsymbol{u}\|}{\|\boldsymbol{u}\|}. \tag{A.3}$$

The resullts (13) and (16) then follow by substituting (A.3) into the main robust performance condition of [30], and specifying both to the case of linear K and M (hence $M|_{\bar{\boldsymbol{u}}} = M$).

Appendix B. Proof of Theorem 3.2

Inserting the form $N = H_{RB}F_m H_{LAD}\boldsymbol{h}_{IRC}$ in the term $N|_{\bar{\boldsymbol{u}}_1}$ gives $N(\boldsymbol{u}+\bar{\boldsymbol{u}}_1) - N\bar{\boldsymbol{u}}_1 = H_{RB}|_{\bar{\boldsymbol{\tau}}_1} F_m(\boldsymbol{\phi}, \dot{\boldsymbol{\phi}})|_{\bar{\boldsymbol{w}}_1} H_{LAD}\boldsymbol{h}_{IRC}|_{\bar{\boldsymbol{z}}_1}\boldsymbol{z}$ where $\bar{\boldsymbol{w}}_1 = H_{LAD}\boldsymbol{h}_{IRC}(A\bar{\boldsymbol{u}}_1)$, $\bar{\boldsymbol{z}}_1 = A\bar{\boldsymbol{u}}_1$ and $\boldsymbol{z} = A\boldsymbol{u}$. Inserting this in the left hand side of (13), together with $M = \overline{H_{RB}F}_m H_{LAD}\bar{\boldsymbol{h}}_{IRC}$, and assuming without loss of generality $\|H_{LAD}\| = 1$, produces

$$\begin{aligned}
\|N|_{\bar{\boldsymbol{u}}_1} - M\| = & \sup_{\substack{\|\boldsymbol{z}\| \neq 0 \\ \boldsymbol{\phi} - \bar{\boldsymbol{\phi}}, \dot{\boldsymbol{\phi}} - \dot{\bar{\boldsymbol{\phi}}} \in \mathcal{L}_2^p[0,T]}} \frac{\|(H_{RB}|_{\bar{\boldsymbol{\tau}}_1} F_m(\boldsymbol{\phi}, \dot{\boldsymbol{\phi}})|_{\bar{\boldsymbol{w}}_1} H_{LAD}\boldsymbol{h}_{IRC}|_{\bar{\boldsymbol{z}}_1} - \overline{H_{RB}F_m}H_{LAD}\bar{\boldsymbol{h}}_{IRC})\boldsymbol{z}\|}{\|\boldsymbol{z}\|} \\
\leq & \sup_{\substack{\|\boldsymbol{z}\| \neq 0 \\ \boldsymbol{\phi} - \bar{\boldsymbol{\phi}}, \dot{\boldsymbol{\phi}} - \dot{\bar{\boldsymbol{\phi}}} \in \mathcal{L}_2^p[0,T]}} \frac{\|(H_{RB}|_{\bar{\boldsymbol{\tau}}_1} F_m(\boldsymbol{\phi}, \dot{\boldsymbol{\phi}})|_{\bar{\boldsymbol{w}}_1} - \overline{H_{RB}F_m})\boldsymbol{z}\|}{\|\boldsymbol{z}\|} \\
& \sup_{\|\boldsymbol{z}\| \neq 0} \frac{\|\bar{\boldsymbol{h}}_{IRC}\boldsymbol{z}\|}{\|\boldsymbol{z}\|} + \sup_{\|\boldsymbol{z}\| \neq 0} \frac{\|(\boldsymbol{h}_{IRC}|_{\bar{\boldsymbol{z}}_1} - \tilde{\boldsymbol{h}}_{IRC}|_{\bar{\boldsymbol{z}}})\boldsymbol{z}\|}{\|\boldsymbol{z}\|} \\
& \sup_{\substack{\|\boldsymbol{z}\| \neq 0 \\ \boldsymbol{\phi} - \bar{\boldsymbol{\phi}}_1, \dot{\boldsymbol{\phi}} - \dot{\bar{\boldsymbol{\phi}}}_1 \in \mathcal{L}_2^p[0,T]}} \frac{\|H_{RB}|_{\bar{\boldsymbol{\tau}}_1} F_m(\boldsymbol{\phi}, \dot{\boldsymbol{\phi}})|_{\bar{\boldsymbol{w}}_1}\boldsymbol{z}\|}{\|\boldsymbol{z}\|}.
\end{aligned} \tag{B.1}$$

Substituting in (13) and rearranging produces the left hand inequality of (17). The right hand inequality follows by taking an alternative partitioning of terms within (B.1).

Appendix C. Proof of Theorem 3.3

Consider the weighted tracking error $\boldsymbol{r}^\star = \min_{\boldsymbol{r}} \|\hat{\boldsymbol{\phi}} - \boldsymbol{\phi}\|_Q^2$ where weight Q realises p channels of $(H(s)^{-1})^* H(s)^{-1}$ with $(\cdot)^*$ the adjoint operator. This has solution

$$\begin{aligned}
\boldsymbol{r}^\star &= \min_{\boldsymbol{r}} \|\hat{\boldsymbol{\phi}} - \boldsymbol{\phi}\|_Q^2 = \min_{\boldsymbol{r}} \|\hat{\boldsymbol{\phi}} - HFX\boldsymbol{r}\|_Q^2 \\
&= \min_{\boldsymbol{r}} \|H^{-1}\hat{\boldsymbol{\phi}} - FX\boldsymbol{r}\|^2 = (FX)^\dagger H^{-1}\hat{\boldsymbol{\phi}}.
\end{aligned}$$

The proposed control action $K_X = C(s)(FX)^\dagger$ realizes $\boldsymbol{r} = C(FX)^\dagger(\hat{\boldsymbol{\phi}} - HFX\boldsymbol{r})$ which, as $n \geq q$, can be rearranged to give $\boldsymbol{r} = (I + CH)^{-1}C(FX)^\dagger HH^{-1}\hat{\boldsymbol{\phi}} = N_w\boldsymbol{r}^\star$. The corresponding closed-loop dynamics are $\boldsymbol{\phi} = HFX\boldsymbol{r} = HFX(I + CH)^{-1}C(FX)^\dagger HH^{-1}\hat{\boldsymbol{\phi}} = N_w(s)FX(FX)^\dagger\hat{\boldsymbol{\phi}}$.

Conflict of interest

No conflict of interest.

References

[1] Pelton T, van Vliet P, Hollands K. Interventions for improving coordination of reach to grasp following stroke: a systematic review. Int J Evid Based Healthc 2012;10(2):89–102.

[2] Hayward K, Barker R, Brauer S. Interventions to promote upper limb recovery in stroke survivors with severe paresis: a systematic review. Disabil Rehabil 2010;32(24):1973–86.

[3] Quandt F, Hummel FC. The influence of functional electrical stimulation on hand motor recovery in stroke patients: a review. Exp Transl Stroke Med 2014;6(1):9.

[4] de Kroon JR, van der Lee JH, Ijzerman MJ, Lankhorst GJ. Therapeutic electrical stimulation to improve motor control and functional abilities of the upper extremity after stroke: a systematic review. Clin Rehabil 2002;16:350–60.

[5] Veerbeek JM, van Wegen E, van Peppen R, van der Wees PJ, Hendriks E, Rietberg M, et al. What is the evidence for physical therapy poststroke? a systematic review and meta-analysis. PLoS ONE 2014;9(2):e87987.

[6] Howlett OA, Lannin NA, Ada L, McKinstry C. Functional electrical stimulation improves activity after stroke: A systematic review with meta-analysis. Arch Phys Med Rehabil 2015;96(5):934–43.

[7] Popović-Maneski L, Kostic M, Bijelic G, Keller T, Mitrovic S, Konstantinovic L, et al. Multi-pad electrode for effective grasping: Design. IEEE Trans Neural Syst Rehabil Eng 2013;21(4):648–54.

[8] Micera S, Keller T, Lawerence M, Morari M, Popovic DB. Wearable neural prosthesis: Restoration od sensory-motor function by transcutaneous electrical stimulation. IEEE Eng Med Biol Mag 2010:64–9.

[9] Heller BW, Clarke AJ, Good TR, Healey TJ, Nair S, Pratt EJ. Automated setup of functional electrical stimulation for drop foot using a novel 64 channel prototype stimulator and electrode array: results from a gait-lab based study. Med Eng Phys 2013;35(1):74–81.

[10] Malešević NM, Maneski LZP, Ilić V, Jorgovanović N, Bijelić G, Keller T, et al. A multi-pad electrode based functional electrical stimulation system for restoration of grasp. J Neuroeng Rehabil 2012;9:66.
[11] O'Dwyer SB, O'Keeffe DT, Coote S, Lyons GM. An electrode configuration technique using an electrode matrix arrangement for fes-based upper arm rehabilitation systems. Med Eng Phys 2006;28:166–76.
[12] Yang K, Freeman CT, Torah RN, Beeby SP, Tudor J. Screen printed fabric electrode array for wearable functional electrical stimulation. Sens Actuators A Phys 2014;213:108–15.
[13] Zirkl M, Sawatdee A, Helbig U, Krause M, Scheipl G, Kraker E, et al. An all-printed ferroelectric active matrix sensor network based on only five functional materials forming a touchless control interface. Adv Mater 2011;23:2069–74.
[14] Kim Y, Kim H, Yoo HJ. Electrical characterization of screen-printed circuits on the fabric. IEEE Trans Adv Packag 2010;33:196–205.
[15] Lawrence M. Transcutaneous electrode technology for neuroprostheses. ETH Zurich; 2009. Ph.D. thesis.
[16] Lymberis A, Paradiso R. Smart fabrics and interactive textile enabling wearable personal applications: R&D state of the art and future challenges. In: Proceedings of the thirtieth annual international IEEE EMBS conference. Vancouver, British Columbia, Canada; 2008. p. 5270–3.
[17] Cherenack K, Zysset C, Kinkeldei T, Münzenrieder N, Tröster G. Woven electronic fibers with sensing and display functions for smart textiles. Adv Mater 2010;22:5178–82.
[18] Cherenack K, v Pieterson L. Smart textiles: Challenges and opportunities. J Appl Phys 2012;112:091301.
[19] Schill O, Rupp R, Pylatiuk C, Schulz S, Reischl M. Automatic adaptation of a self-adhesive multi-electrode array for active wrist joint stabilization in tetraplegic SCI individuals. In: Proceedings of the 2009 IEEE toronto international conference science and technology for humanity (TIC-STH); 2009. p. 708–13.
[20] Keller T, Lawrence M, Kuhn A, Morari M. New multi-channel transcutaneous electrical stimulation technology for rehabilitation. In: Proceedings of the twenty-eighth IEEE EMBS annual international conference. New York; 2006. p. 194–7.
[21] Popović DB, Popović MB. Automatic determination of the optimal shape of a surface electrode: Selective stimulation. J Neurosci Methods 2009;178(1):174–81.
[22] Malešević N, Popović L, Bijelic G, Kvascev G. Muscle twitch responses for shaping the multi-pad electrode for functional electrical stimulation. J Autom Control 2010;20:53–7.
[23] Freeman CT. Control system design for electrical stimulation in upper limb rehabilitation. Springer International Publishing; 2016. . 176 pages. doi:10.1007/978-3-319-25706-8.
[24] Valero-Cuevas FJ. A mathematical approach to the mechanical capabilities of limbs and fingers. Progr Motor Control 2009;629:619–33.
[25] Feldman AG, Latash M. Testing hypotheses and the advancement of science: recent attempts to falsify the equilibrium point hypothesis. Brain Res 2005;161:91–103.
[26] Vodovnik BL, Bowman R, Bajd T. Dynamics of a spastic knee joint. Med Biol Eng Comput 1984;22:63–9.
[27] Brend OW, Freeman CT, French M. Multiple model adaptive control of functional electrical stimulation. IEEE Trans Control Syst Technol 2015;23(5):1901–13.
[28] Freeman CT. Electrode array-based electrical stimulation using ILC with restricted input subspace. Control Eng Pract 2014;23(2):32–43.
[29] Freeman CT, French M. Estimation based multiple model iterative learning control. In: Proceedings of the fifty-fourth IEEE conference on decision and control; 2015. p. 6075–80.
[30] Georgiou TT, Smith MC. Robustness analysis of nonlinear feedback systems: An input–output approach. IEEE Trans Autom Control 1997;42(9):1200–21.